Hyperspectral Imaging for In-Vivo/Ex-Vivo Tissue Analysis of Human Brain Cancer

Raquel Leon[†,*,a], Sofia H. Gelado[†,b,α], Himar Fabelo[a,g], Samuel Ortega[a,c], Laura Quintana[a], Adam Szolna[d], Juan F. Piñeiro[d], Francisco Balea-Fernandez[e], Jesus Morera[d], Bernardino Clavo[f,g], Gustavo M. Callico[a]

[a]Research Institute for Applied Microelectronics, Univ. of Las Palmas de Gran Canaria, Spain.
[b]Dept. of Biomedical Engineering, Univ. of Glasgow, UK.
[c]Nofima, Norwegian Institute of Food Fisheries and Aquaculture Research, Tromsø, Norway.
[d]Dept. of Neurosurgery, Univ. Hospital Doctor Negrin of Gran Canaria, Spain.
[e]Univ. of Las Palmas de Gran Canaria, Spain.
[f]Research Unit, Univ. Hospital Doctor Negrin of Gran Canaria, Spain.
[g]Instituto de Investigación Sanitaria de Canarias (IISC), Spain.
[†]Equal contribution. *E-mail: slmartin@iuma.ulpgc.es.
[α]This work was conducted while this author was doing a research internship at the Research Institute for Applied Microelectronics

ABSTRACT

Accurate identification of tumor boundaries during brain cancer surgery determines the quality of life of the patient. Different intraoperative guidance tools are currently employed during the resection tumor but having several limitations. Hyperspectral imaging (HSI) is arising as a label-free and non-ionizing technique that could assist neurosurgeons during surgical procedures. In this paper, an analysis between in-vivo and ex-vivo human brain tumor samples using HSI has been performed to evaluate the correlation between both types of samples. Spectral ratios of the oxygenated and deoxygenated hemoglobin were employed to distinguish between normal tissue, tumor tissue and blood vessels. A database composed by seven in-vivo and fourteen ex-vivo hyperspectral images obtained from seven different patients diagnosed with glioblastoma Grade IV, metastatic secondary breast cancer, meningioma Grade I and II, and astrocytoma (glioma) Grade II. 44,964 pixels labeled pixels were employed in this work. The proposed method achieved discrimination between different tissue types using the proposed spectral ratio. Comparison between in-vivo and ex-vivo samples indicated that ex-vivo samples generate higher hemoglobin ratios. Moreover, vascular enhanced maps were generated using the spectral ratio, targeting real-time intraoperative surgical assistance.

Keywords: Brain tumor, cancer surgery, hyperspectral imaging, intraoperative imaging, hemoglobin ratio.

1. INTRODUCTION

One of the main causes of mortality and morbidity in the population is caused by brain cancer, especially in children.[1,2] Brain tumors are divided into two groups depending on the cancer malignity: low-grade (LG), covering grades I and II, and high-grade (HG), including grades III and IV. An accurate identification of the boundaries between tumor and normal tissue during resection determine prolonged survival. Several intraoperative guidance tools are employed during surgery, such as intraoperative Image Guided Stereotactic (IGS) neuronavigation, intraoperative Magnetic Resonance Imaging (iMRI), or fluorescent tumor markers like 5-aminolevulinic acid (5-ALA). However, these technologies present several limitations.[3,4]

Hyperspectral (HS) imaging (HSI) is a label-free and non-ionizing technology that combines conventional imaging and spectroscopy in one single mode, obtaining the spatial and the spectral information from a scene simultaneously by using halogen illumination.[5] Different industrial applications employ this technology since many years[6], while in the medical field the use of HSI has been widely investigated.[7] Brain tumor identification has been investigated by this research group employing HSI.[8] Spectral ratios have been used to discriminate between different types of tissues in a variety of imaging methods including diffuse reflectance spectroscopy[9] and HSI.[10] In HSI, the spectral band ratio R545/R560 has been applied for the identification of brain ischemia in rats. Fu *et al.* proposed the use of the ratio between 545 nm isosbestic band of oxy-Hb (oxygenated hemoglobin) and deoxy-Hb (deoxygenated hemoglobin), which is independent of changes in saturation and the 560 nm band, at which the largest difference between oxy-Hb and deoxy-Hb occurs.[10] The ratio reflects a maximized difference between deoxy-Hb and oxy-Hb. Their study demonstrated the use of the R545/R560 spectral ratio

on HSI for the identification of brain ischemia as well as the application of classification thresholds based on these ratios to distinguish infarcted from normal brain tissue.[10]

In this work, the R545/R560 spectral ratio has been employed to perform a quantitative evaluation of the in-vivo and ex-vivo tumor tissue samples, as well as to qualitatively evaluate the generation of heatmaps and vascular enhanced maps of in-vivo tissue, targeting real-time surgical guidance.

2. MATERIALS AND METHODS

2.1 In-vivo and ex-vivo HS human brain cancer database

The in-vivo and ex-vivo human brain images were acquired using an intraoperative HS acquisition system. This system was composed by a push-broom HS camera, an illumination system, and a scanning platform.[11] The HS camera based on visible and near infrared (VNIR) covers the spectral range between 400 and 1,000 nm. It can capture 1,004 spatial pixels with a pixel pitch of 7.4 µm and 826 spectral bands with a spectral sampling of 0.73 nm and a spectral resolution of 2–3 nm. The HS camera was coupled to the scanning platform, which provided the necessary movement to generate the HS cube, due to the push-broom technique. The illumination system was based on a quartz tungsten halogen (QTH) lamp of 150 W connected to a cold light emitter through an optical fiber to avoid the high temperatures of the QTH lamp in the exposed brain surface.

The HSI database was composed by seven in-vivo and fourteen ex-vivo HS images obtained from seven different patients diagnosed with glioblastoma Grade IV, metastatic secondary breast cancer, meningioma Grade I and II, and astrocytoma (glioma) Grade II. The HS images were acquired at the University Hospital of Las Palmas de Gran Canaria Doctor Negrin, Spain, from patients that underwent craniotomy for resection of intra-axial brain tumors. The study protocol and consent procedures were approved by the *Comité Ético de Investigación Clínica-Comité de Ética en la Investigación (CEIC/CEI)* of University Hospital Doctor Negrin and written informed consent was obtained from all subjects. The procedure to generate the database was as follows. Once craniotomy and opening of the dura was performed, the operating surgeon identified the approximate location of normal brain parenchyma and tumor, and the imaging operator captured the HS image. Next, the tumor tissue was resected and the ex-vivo tissue was captured within the operating theater. Finally, a biopsy of the tumor was analyzed by a pathologist, determining the tumor type and grade. Table 1 summarize the database where 44,964 pixels were labeled from in-vivo images with three different tissue classes: 10,977 pixels of *tumor tissue* (TT), 17,925 pixels of *normal tissue* (NT) and 16,062 pixels of *blood vessels* (BV).

Table 1. Summary of the labeled dataset. (*) Image IDs without labeled pixels correspond to the ex-vivo HS tumor samples.

Patient ID	**Image ID**	**Image Size (height × width × bands)**	**#Labeled Pixels**			**Diagnosis**
			NT	**TT**	**HT**	
P8	C2	480 × 553 × 826	2,187	138	1,000	Glioblastoma Grade IV
	C3*	158 × 196 × 826	-	-	-	
P15	C1	376 × 494 × 826	1,251	2,046	4,089	Glioblastoma Grade IV
	C2*	146 × 182 × 826	-	-	-	
	C3*	326 × 270 × 826	-	-	-	
P21	C1	452 × 334 × 826	2,663	1,221	2,325	Secondary Breast
	C3*	215 × 223 × 826	-	-	-	
	C4*	214 × 229 × 826	-	-	-	
P50	C1	565 × 533 × 826	2,116	1,091	620	Meningioma Grade I
	C2*	431 × 412 × 826	-	-	-	
	C3*	518 × 693 × 826	-	-	-	
56	C1	446 × 598 × 826	1,346	4,081	2,200	Astrocytoma (glioma) Grade II
	C3*	228 × 197 × 826	-	-	-	
	C4*	210 × 213 × 826	-	-	-	
57	C1	440×535×826	1,773	771	1,263	Secondary Breast
	C3*	159×140×826	-	-	-	
	C4*	169×148×826	-	-	-	
P58	C2	721×752×826	6,589	1,629	4,565	Meningioma Grade II
	C3*	330×346×826	-	-	-	
	C4*	455×338×826	-	-	-	
	C5*	390×205×826	-	-	-	
Total			**17,925**	**10,977**	**16,062**	

The labelling was performed using a semiautomatic labelling tool based on Spectral Angle Mapper algorithm to generate the ground-truth maps.[12] Ex-vivo images were not labeled. Figure 1 shows the in-vivo HS images used in this work together with their corresponding ground-truth maps. In these maps, normal, tumor and blood vessel pixels are represented in green, red, and blue color respectively. Black pixels correspond to the background labeled in the images (not employed in this work) and white pixels are the non-labeled pixels. Figure 2 shows the synthetic RGB images of the ex-vivo HS images where it is worth noticing that images from P21 and P56 were captured with different focus. This data was employed to determine if this focus differences could affect the results.

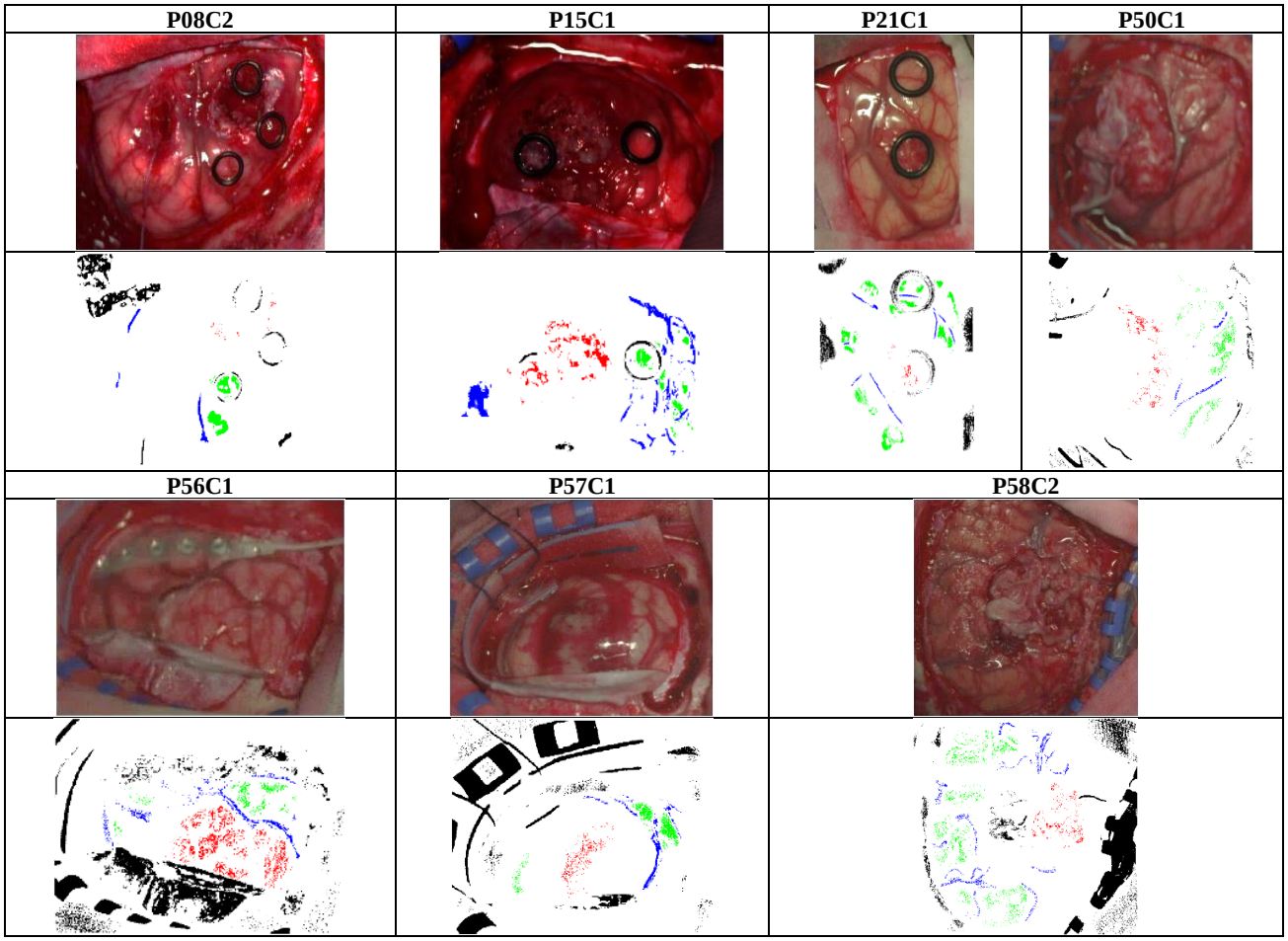

Figure 1. Synthetic RGB images and ground-truth maps of the in-vivo human brain HS images employed in this study.

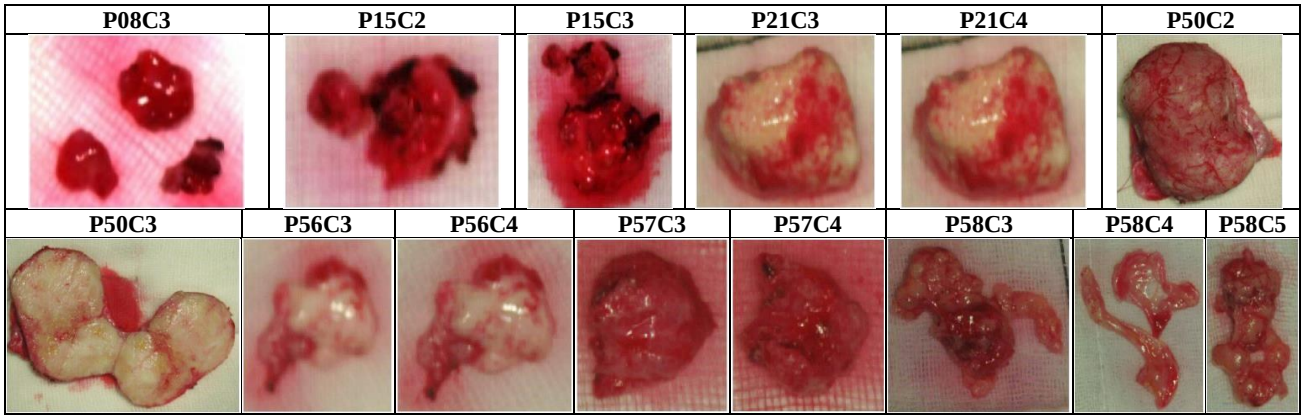

Figure 2. Synthetic RGB images of the ex-vivo human brain tumor HS images employed in this study.

2.2 Data pre-processing

The HS images obtained with the HS intraoperative system were pre-processed applying data calibration, spectral noise reduction and band removal. The HS images were calibrated following Eq. (1), where CI is the calibrated image, RI is the raw image, and WI and DI are the white and dark reference images, respectively. The white reference image was acquired using a standard white reference tile that reflects the 99% of the incident light, in the same illumination conditions that the image was captured. The dark reference image was obtained by keeping the camera shutter closed. A spectral noise reduction algorithm was applied to the data by using a moving average filter for reducing the high-frequency noise with a window of five data points. Finally, due to the low performance of the HS sensor in the lower and higher spectral bands, the spectral ranges from 400 to 440 nm and from 909 to 1,000 nm were removed. At the end, the resulting HS cube was composer of 645 spectral bands in the spectral range comprised between 440 and 909 nm. The statistical analysis was performed using the absorbance values of the spectral signatures. Therefore, absorbance (A) was computed following Eq. (2), where R is the reflectance value and λ represent each wavelength. Figure 3 shows an example of a spectral signature at the different steps of the pre-processing chain.

$$CI = \frac{RI - DI}{WI - DI} \tag{1}$$

$$A(\lambda) = -\log\left(R(\lambda)\right) \tag{2}$$

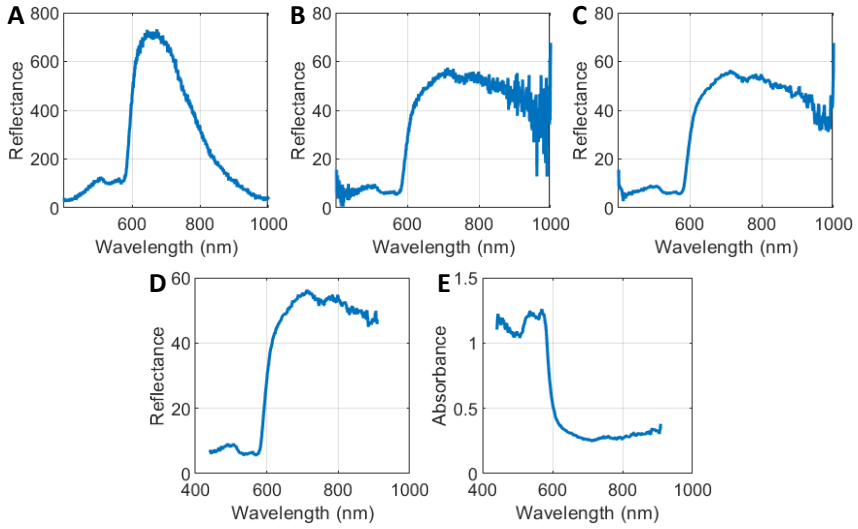

Figure 3. Example of a spectral signature in the different steps of the pre-processing chain. (A) Raw spectrum; (B) Calibrated spectrum; (C) Spectrum with the spectral noise reduction applied; (D) Final spectrum after lower/higher bands removal; (E) Final spectrum in converted to absorbance values.

2.3 Diffuse absorbance spectral ratio processing framework

The proposed method for computing the absorbance spectral ratio and perform the comparison between the in-vivo and ex-vivo tissue samples is composed by different stages as shown in Figure 4.

First, the raw HS images captured with the intraoperative acquisition system (Figure 4.A) were pre-processed and converted to absorbance to perform the spectral analysis between the corresponding in-vivo and ex-vivo HS images (Figure 4.B and C, respectively). Then, on the one hand, the in-vivo HS images were labeled to generate a ground-truth map (Figure 4.D) where the identification of the different tissue classes in the exposed brain surface is achieved (as explained in Section 2.1). On the other hand, a clustering algorithm was employed in the ex-vivo images to identify different regions in the tissue sample in an unsupervised way (Figure 4.E). Principal Component Analysis (PCA) was used to perform the segmentation of the ex-vivo tissue using the K-means unsupervised clustering algorithm. In order to determine the optimal number of clusters (*K*), three clustering evaluation methods were employed (Calinski Harabasz,[13] Davies Bouldin,[14] and Silhouette[15]) in each HS image, independently. This cluster evaluation was performed without taking account the background of the image (mainly composed by the white gauze where the tissue sample was placed). To achieve this, a

manually segmentation mask of each ex-vivo samples was created. After finding the optimal *K* value, the K-means algorithm was applied using this value to generate the ex-vivo clustering maps. The spectral signatures from such regions were then extracted for performing the analysis of the spectral signatures independently in each cluster and compare them with the corresponding labeled data from the in-vivo HS images (Figure 4.F). Additionally, such data was employed to perform a statistical comparison using the proposed R545/R560 spectral ratio method (Figure 4.G)

Finally, HbRatio-based heatmaps of the in-vivo and ex-vivo samples were generated using the R545/R560 spectral ratio (Figure 4.H) and a qualitative evaluation of these samples was performed. In order to reduce noise in the heatmaps, a Gaussian smoothing filter was applied using a fixed sigma value ($sigma = 1$). In the in-vivo HbRatio-based heatmaps a qualitative evaluation of the different tissue structure was performed. In addition, an analysis of the distribution of R540/R560 in labeled blood vessel pixels was employed to automatically enhance their structures in the in-vivo images (Figure 4.I). The first and third quartiles of the distribution acted as the limits to produce these vascular enhanced maps.

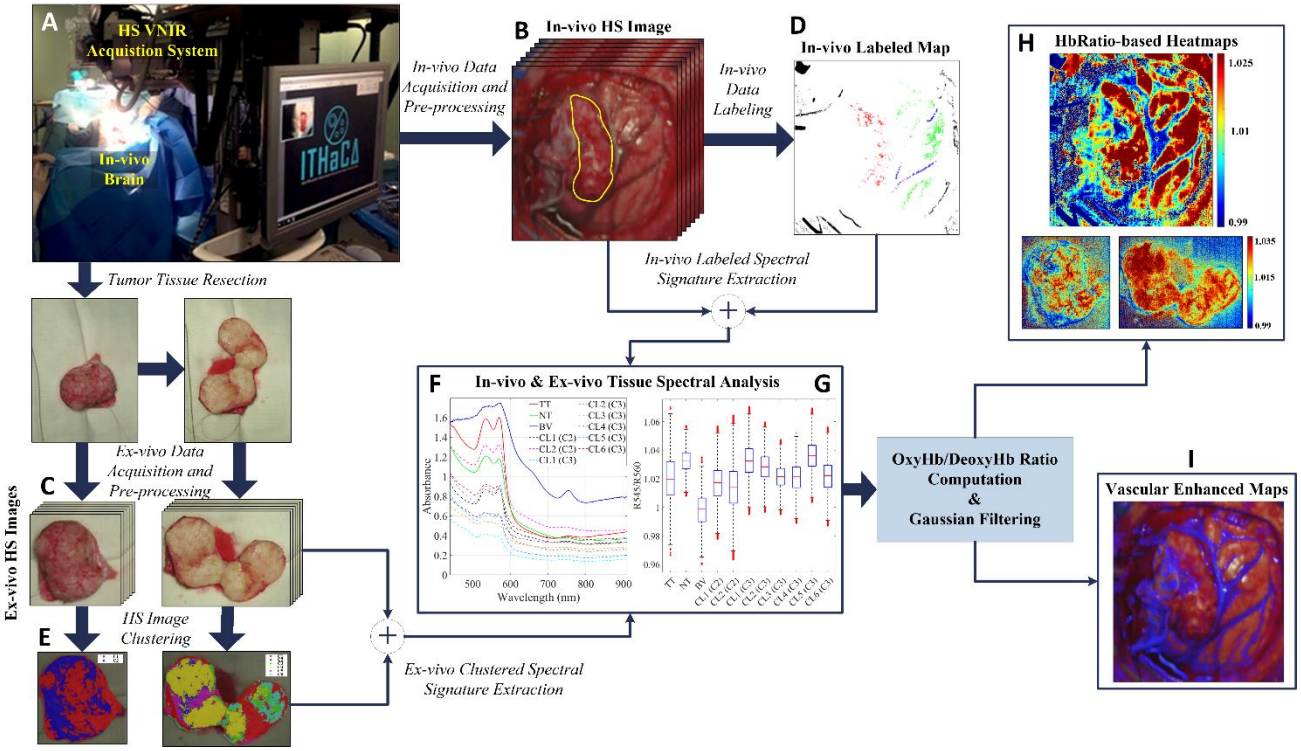

Figure 4. Block diagram of the proposed diffuse absorbance spectral ratio processing framework.

3. EXPERIMENTAL RESULTS

3.1 Unsupervised clustering of ex-vivo tumor samples

The K-means algorithm was applied to the ex-vivo HS images in order to segment the samples into different clusters. Cluster evaluation was performed in each HS image. P08C3 is composed by three pieces and each piece was consider as an independent image for the analysis. After applying the three cluster evaluation methods, the optimal number of clusters obtained was two in almost all HS ex-vivo image, except for P50C3 (six clusters), and P58C4 and P58C5 (five clusters). Figure 5 shows the ex-vivo segmentation maps. Additionally, it is worth noticing that P21C3 and P21C4, which were captured with different focus, obtained similar segmentation maps.

3.2 Spectral comparison among in-vivo and ex-vivo samples

The in-vivo and ex-vivo tissue spectral analysis was performed evaluating the absorbance values in the different tissue samples. Figure 6 shows the mean spectral signatures from each class (NT, TT, and BV) of the in-vivo HS images (solid lines) and the different clusters obtained in the corresponding ex-vivo HS images (dashed lines).

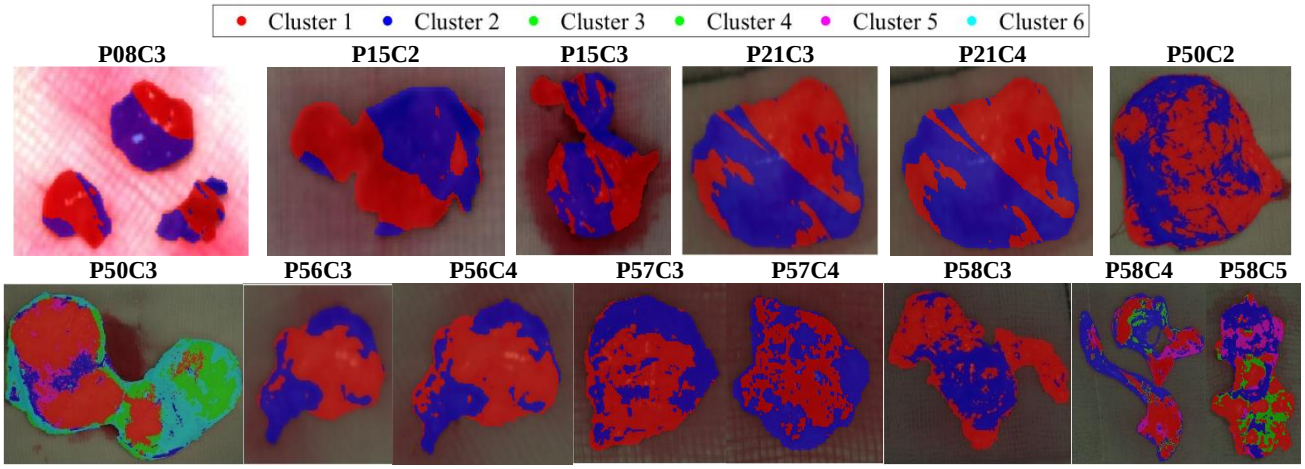

Figure 5. Ex-vivo segmentation maps applying K-means algorithm (colors are randomly assigned).

It can be observed that in the in-vivo samples the absorbance values of BV pixels between 500 and 600 nm are higher than in tumor and normal tissue, having normal tissue the lowest absorbance values. The ex-vivo spectral signatures have different absorbance values depending on the clusters obtained in the HS images. This can be related to differences between tissue types in the resected sample, which can involve tumor and the surrounding healthy tissue in some cases. Ex-vivo spectral signatures from P21C3 and P21C4 (Figure 6.C) are overlapping indicating, in this case, that having a slightly different focus does not affect the spectral signature. However, in P56C3 and P56C4 (Figure 6.E) the amplitudes are similar but not overlapped, this can be produced due to both images have higher differences in focus than P21.

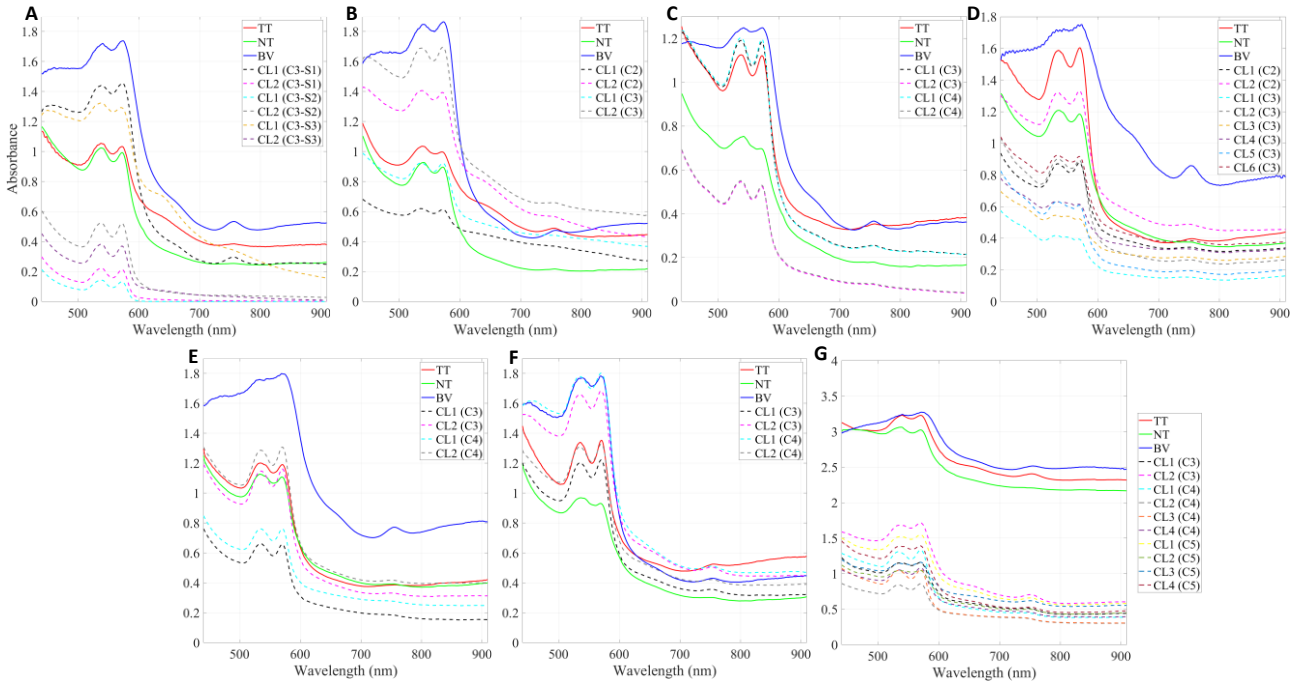

Figure 6. Mean spectral signatures of the different classes labelled in the in-vivo samples (solid lines) and the different clusters (dashed lines) obtained from the corresponding resected ex-vivo tissue (from different captures). (A) P08, (B) P15, (C) P21, (D) P50, (E) P56, (F) P57, and (G) P58. TT: Tumor Tissue; NT: Normal Tissue; BV: Blood Vessels; CL: Cluster; C: Capture; S: Segment from the capture in the cases where there are several ex-vivo tissue in the same capture.

3.3 Statistical analysis of the R545/R560 spectral ratio between in-vivo and ex-vivo samples

Figure 7 shows the boxplots of the R545/R560 spectral ratios obtained in the different tissue types. These results show that, in the in-vivo samples, NT achieved higher ratios followed by TT and BV. Additionally, it can be observed that higher ratio values were obtained in the ex-vivo data respect to the in-vivo data. However, ex-vivo data present high interquartile rages (IQR). From these results, it is possible to observe that lower ratio values involve higher hemoglobin (Hb) contributions. In this sense, it is possible to observe that in the in-vivo samples, as expected, the blood vessel class has the lowest ratio values, while the normal class has the highest. In the case of the tumor class, the ratio values are lower than the normal class due to the hypervascularization produced by the tumor.

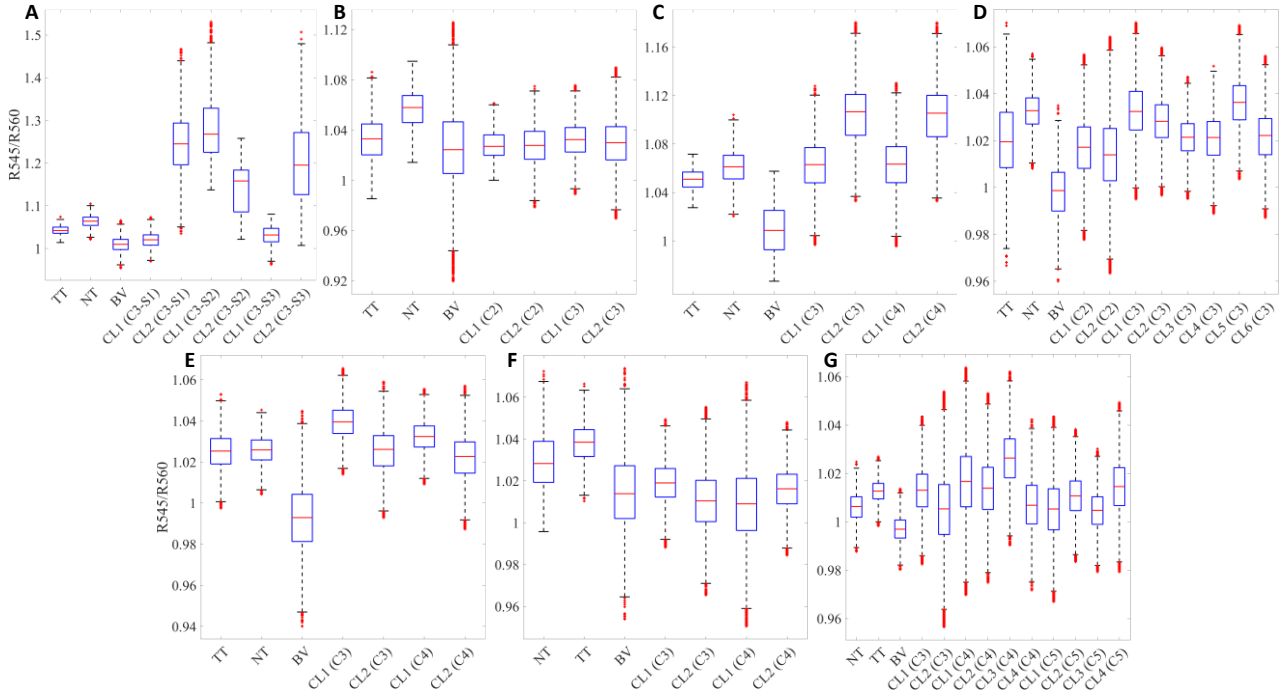

Figure 7. Boxplots of the R545/R560 spectral ratios from the different classes labelled in the in-vivo samples and the different clusters obtained from the corresponding resected ex-vivo tissue (from different captures). (A) P08, (B) P15, (C) P21, (D) P50, (E) P56, (F) P57, and (G) P58. TT: Tumor Tissue; NT: Normal Tissue; BV: Blood Vessels; CL: Cluster; C: Capture; S: Segment from the capture in the cases where there are several ex-vivo tissue in the same capture.

3.4 In-vivo HbRatio-based heatmaps and vascular enhanced maps

Using the R545/R560 spectral ratios and the first and third quartiles as threshold points, HbRatio-based heatmaps and vascular enhanced maps were generated as shown in Figure 8. A Gaussian smoothing filter was applied to the HbRatio-based heatmaps in order to reduce the spatial noise in the results. In the vascular enhanced maps, blood vessels were. In general, well delimited using such spectral ratios. However, in some cases, background elements were identified as vascular, for example in P15C2 and P57C1. In any case, this background elements can be easily identified by the operating surgeon's naked eye.

4. CONCLUSION

To the best of our knowledge, the work presented in this paper employs, for the first time, a discrimination of different in-vivo human brain tissue structures based on Hb ratios using HSI. The ratio reflects a maximized difference between deoxy-Hb and oxy-Hb. In addition, HbRatio-based heatmaps and vascular enhanced maps were obtained using the first and third quartiles of R45/R60 spectral ratio. This work analyzes the correlation between ex-vivo and in-vivo samples of human brain tissue that, to the best of our knowledge, has not been carried out in the literature. This correlation was performed after analyzing the optimal cluster values in the ex-vivo samples to extract the spectral signatures.

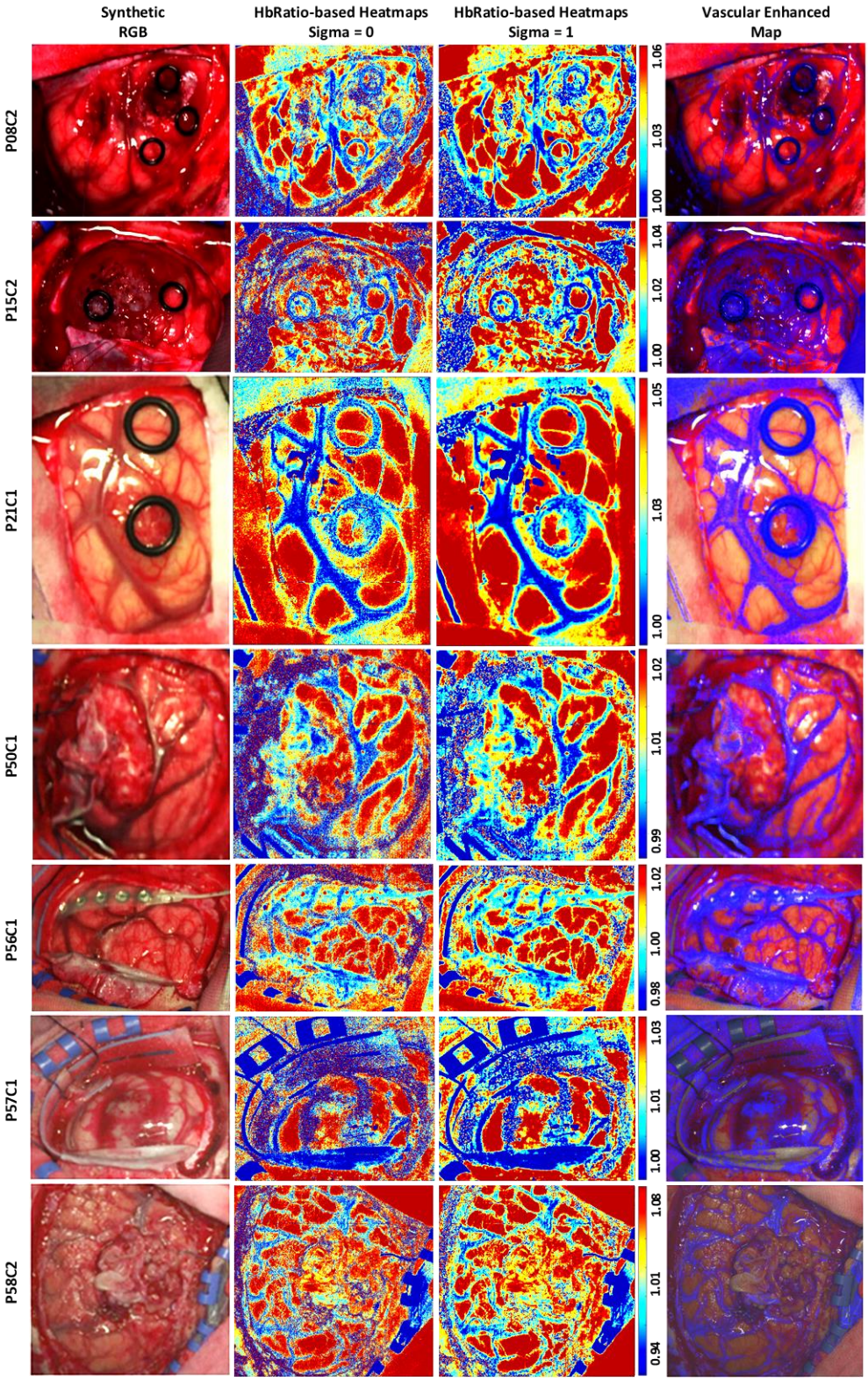

Figure 8. Synthetic RGB images, HbRatio-based heatmaps (before and after applying Gaussian smoothing filter) and vascular enhanced maps (obtained with first and third quartiles of R545/R560 spectral ratio) from the seven HS in-vivo images from the seven different patients.

This work would allow the development of a real-time intraoperative system for enhanced surgical guidance and blood flow monitoring. The system could be based on an HS camera that captures only the spectral bands used to calculate the Hb ratio, reducing the acquisition time and the high computation requirements for processing large number of spectral bands. By reducing the spectral range, the spatial resolution could increase, improving also the definition of the generated maps. In addition, the identification of the blood vessels in the enhanced vascular maps could help to improve the identification of tumor areas during surgical procedures, by reducing the number of classes to be differentiated by a machine learning classifier. This fact, in addition with the identification of the parenchymal area of the surgical scene could achieve a binary classification between tumor and normal tissue that have been demonstrated to be more precise than a four class-classification.[8] For this reason, future works will involve the use of deep learning techniques to identify parenchymal areas in the HS images, as well as the use of the proposed enhanced vascular maps to identify blood vessel, allowing a later binary classification of the brain tissue between tumor and normal parenchymal tissue.

DISCLOSURES

The authors have no relevant financial interests in this article and no potential conflicts of interest to disclose. The study protocol and consent procedures were approved by the *Comité Ético de Investigación Clínica-Comité de Ética en la Investigación (CEIC/CEI)* of University Hospital Doctor Negrin and written informed consent was obtained from all subjects.

ACKNOWLEDGMENTS

This work has been supported in part by the European Commission through the H2020-EU.3.1.4.2., European Project WARIFA (Watching the risk factors: Artificial intelligence and the prevention of chronic conditions) under Grant Agreement 101017385, and by the Spanish Government and European Union (FEDER funds) as part of support program in the context of TALENT-HExPERIA (HypErsPEctRal Imaging for Artificial intelligence applications) project, under contract PID2020-116417RB-C42. Additionally, this work was completed while Raquel Leon was beneficiary of a predoctoral grant given by the "Agencia Canaria de Investigación, Innovación y Sociedad de la Información (ACIISI)" of the "Consejería de Economía, Conocimiento y Empleo", which is part-financed by the European Social Fund (FSE) (POC 2014-2020, Eje 3 Tema Prioritario 74 (85%)). Finally, this work was completed while Himar Fabelo was beneficiary of the FJC2020-043474-I funded by MCIN/AEI/10.13039/501100011033 and by the European Union "NextGenerationEU/PRTR".

REFERENCES

[1] Patel, A. P., Fisher, J. L., Nichols, E., Abd-Allah, F., Abdela, J., Abdelalim, A., Abraha, H. N., Agius, D., Alahdab, F., Alam, T., Allen, C. A., Anber, N. H., Awasthi, A., Badali, H., Belachew, A. B., Bijani, A., Bjørge, T., Carvalho, F., Catalá-López, F., et al., "Global, regional, and national burden of brain and other CNS cancer, 1990–2016: a systematic analysis for the Global Burden of Disease Study 2016," Lancet Neurol. **18**(4), 376–393 (2019).

[2] Siegel, R. L., Miller, K. D., Fuchs, H. E. and Jemal, A., "Cancer Statistics, 2021," CA. Cancer J. Clin. **71**(1), 7–33 (2021).

[3] Gerard, I. J., Kersten-Oertel, M., Petrecca, K., Sirhan, D., Hall, J. A. and Collins, D. L., "Brain shift in neuronavigation of brain tumors: A review," Med. Image Anal. **35**, 403–420 (2017).

[4] Schwake, M., Schipmann, S., Müther, M., Köchling, M., Brentrup, A. and Stummer, W., [5-ALA fluorescence–guided surgery in pediatric brain tumors—a systematic review], Springer-Verlag Wien, 1099–1108 (2019).

[5] Li, Q., He, X., Wang, Y., Liu, H., Xu, D. and Guo, F., "Review of spectral imaging technology in biomedical engineering: achievements and challenges," J. Biomed. Opt. **18**(10), 100901 (2013).

[6] Calin, M. A., Parasca, S. V., Savastru, D. and Manea, D., "Hyperspectral Imaging in the Medical Field: Present and Future," Appl. Spectrosc. Rev. **49**(6), 435–447 (2014).

[7] Halicek, M., Fabelo, H., Ortega, S., Callico, G. M. and Fei, B., "In-Vivo and Ex-Vivo Tissue Analysis through Hyperspectral Imaging Techniques: Revealing the Invisible Features of Cancer," Cancers (Basel). **11**(6), 756 (2019).

[8] Fabelo, H., Halicek, M., Ortega, S., Shahedi, M., Szolna, A., Piñeiro, J. F., Sosa, C., O'Shanahan, A. J., Bisshopp, S., Espino, C., Márquez, M., Hernández, M., Carrera, D., Morera, J., Callico, G. M., Sarmiento, R.

and Fei, B., “Deep Learning-Based Framework for In Vivo Identification of Glioblastoma Tumor using Hyperspectral Images of Human Brain,” Sensors **19**(4), 920 (2019).
[9] N, S., JR, M., SS, T., A, M., P, S. and J, M., “Oral cancer detection using diffuse reflectance spectral ratio R540/R575 of oxygenated hemoglobin bands,” J. Biomed. Opt. **11**(1), 014018 (2006).
[10] Fu, C., Ma, K., Li, Z., Wang, H., Chen, T., Zhang, D., Wang, S., Mu, N., Yang, C., Zhao, L., Gong, S., Feng, H. and Li, F., “Rapid, label-free detection of cerebral ischemia in rats using hyperspectral imaging,” J. Neurosci. Methods **329**, 108466 (2020).
[11] Fabelo, H., Ortega, S., Lazcano, R., Madroñal, D., M. Callicó, G., Juárez, E., Salvador, R., Bulters, D., Bulstrode, H., Szolna, A., Piñeiro, J., Sosa, C., J. O’Shanahan, A., Bisshopp, S., Hernández, M., Morera, J., Ravi, D., Kiran, B., Vega, A., et al., “An Intraoperative Visualization System Using Hyperspectral Imaging to Aid in Brain Tumor Delineation,” Sensors **18**(2), 430 (2018).
[12] Fabelo, H., Ortega, S., Szolna, A., Bulters, D., Pineiro, J. F., Kabwama, S., J-O’Shanahan, A., Bulstrode, H., Bisshopp, S., Kiran, B. R., Ravi, D., Lazcano, R., Madronal, D., Sosa, C., Espino, C., Marquez, M., De La Luz Plaza, M., Camacho, R., Carrera, D., et al., “In-Vivo Hyperspectral Human Brain Image Database for Brain Cancer Detection,” IEEE Access **7**, 39098–39116 (2019).
[13] Caliński, T. and Harabasz, J., “A Dendrite Method Foe Cluster Analysis,” Commun. Stat. **3**(1), 1–27 (1974).
[14] Davies, D. L. and Bouldin, D. W., “A Cluster Separation Measure,” IEEE Trans. Pattern Anal. Mach. Intell. **PAMI-1**(2), 224–227 (1979).
[15] Rousseeuw, P. J., “Silhouettes: A graphical aid to the interpretation and validation of cluster analysis,” J. Comput. Appl. Math. **20**(C), 53–65 (1987).